Bandgap bowing in a zero-dimensional hybrid halide perovskite derivative: spin-orbit coupling versus lattice strain†

Soumyo Chatterjee,[1] Julia Payne,[2] John T. S. Irvine,[2] and Amlan J. Pal*[1]

[1] *School of Physical Sciences, Indian Association for the Cultivation of Science, Jadavpur, Kolkata 700032, India*

[2] *School of Chemistry, University of St Andrews, Scotland KY16 9ST, UK*

We have considered a zero-dimensional hybrid halide perovskite derivative system, namely $MA_3(Sb_{1-x}Bi_x)_2I_9$, to study the bandgap dependence on metal substitution. Similar to tin-lead mixed halide perovskites ($MASn_{1-x}Pb_xI_3$), composition dependence of optical bandgap in the $MA_3(Sb_{1-x}Bi_x)_2I_9$ solid-state alloys showed evidence of a quadratic (bow-like) behavior where an intermediate compound containing equimolar contribution of antimony and bismuth, $MA_3(Sb_{0.5}Bi_{0.5})_2I_9$ offered a narrowest bandgap of around 1.90 eV; this is markedly lower than the bandgap of the end members $MA_3Sb_2I_9$ (2.36 eV) and $MA_3Bi_2I_9$ (2.16 eV). In addition, we have observed the bowing in the transport gap of $MA_3(Sb_{1-x}Bi_x)_2I_9$ that has been derived from scanning tunneling spectroscopy and density of states spectra thereof. To explain the underlying mechanism, we speculate that an antagonism between spin orbit coupling and its competing component, namely lattice strain, may have led to this bow-like nature in both optical and transport gaps. The band-diagram of heterojunctions based on $MA_3(Sb_{1-x}Bi_x)_2I_9$ accordingly depended on the metal-composition; solar cell characteristics of the heterojunctions followed the change in bandgap, morphology, and also the exciton binding energy.

Keywords: Bandgap bowing, zero-dimensional hybrid halide perovskite derivative, bismuth substitution at antimony sites, spin-orbit coupling, lattice strain, exciton binding energy.

E-mail: sspajp@iacs.res.in

1. Introduction

In the quest for lead-free solar energy materials, perovskite-like compounds containing trivalent metal cations, such as bismuth (Bi^{3+}) or antimony (Sb^{3+}), have recently become a topic of interest.[1,2] Apart from addressing the toxicity issue associated with traditional lead-based perovskites, these potential alternatives have shown superior stability under ambient condition along with promising light harvesting properties.[3] These materials are typically expressed by a generic structural formula $A_3B_2X_9$, where, A and X are a monovalent cation and a halogen, respectively, whereas, for the B-sites, trivalent group-V elements (Bi^{3+} or Sb^{3+}) have been the choice due to their isoelectronic configuration (s^2p^0) to lead (Pb^{2+}) and presence of lone-pair states.[4,5] Depending on the choice of the A-site cation, these $A_3B_2X_9$ compounds can exist in a couple of typical polymorphs,[6] namely, a two-dimensional (2D) layered structure (for A = rubidium, cesium) or a zero-dimensional (0D) dimer-like structure (for A = methylammonium), where, formation of the latter one is thermodynamically favored.[7,8] However, due to a strong dimensional reduction in dimer-phase, $A_3B_2X_9$ compounds namely, methylammonium bismuth iodide ($MA_3Bi_2I_9$) and methylammonium antimony iodide ($MA_3Sb_2I_9$), are unfortunately associated with some intrinsic limitations including wide optical bandgap, inferior carrier transport and strong quantum confinement effect making them less favorable for photovoltaic applications.[9,10] With limited option of suitable trivalent metal cations for the B-sites, efforts to bring down the optical bandgap have mostly been focused on heterovalent substitutions at the metal and halogen sites,[11,12] whereas, an improved carrier transport has been reported in the layered phase.[8] Conversely, due to a smaller effective ionic radius (r_{ion}) of antimony than bismuth (r_{ion} of Sb^{3+} and Bi^{3+} are 76 and 103 pm, respectively), $MA_3Sb_2I_9$ offered a lower exciton binding energy than $MA_3Bi_2I_9$.[10] In spite of such strategies, power conversion efficiency (PCE) of solar cells based on these lead-free alternatives is yet to flourish.[1,10]

Solid-state alloying has been a widely used tool to address some distinct shortcomings of halide perovskites, such as, restricted range of optical bandgap and chemical stability.[13,14] With bismuth and antimony being the ideal options for a trivalent element at the B-sites, the search for a route to lower the bandgap of $MA_3B_2I_9$ compounds by forming $MA_3(Sb_{1-x}Bi_x)_2I_9$ solid state alloys is apparently blocked if a linear dependence of bandgap on the composition is maintained following Vegard's law. In this respect, a nonmonotonic and nonlinear (quadratic) characteristic has been recently observed in $MAPbI_3$-based perovskite alloys.[15] The effect, which is commonly termed as "bandgap bowing", led to the achievement of a

lower bandgap in the intermediate compounds of $MASn_{1-x}Pb_xI_3$ solid solution than the end members. To be precise, in such perovskite alloys, an equimolar combination of tin and lead ($x = 0.5$) has offered the narrowest bandgap of around 1.10 eV, whereas, bandgaps of the end members $MAPbI_3$ and $MASnI_3$ were estimated to be 1.55 and 1.30 eV, respectively.[16] While the phenomenon has a strong technological significance, the origin of such a bandgap bowing is yet to be clearly understood. It has been proposed so far through first principle calculations that either an energy mismatch between the atomic orbitals of the parent materials or a competing effect of spin-orbit coupling in the electronic structure and modification in the crystal structure due to lattice-strains could be responsible for the so-called bowing effect.[15]

In this work, we accordingly aimed to lower the bandgap of zero-dimensional $MA_3Sb_2I_9$ perovskite derivative through isovalent metal substitution by bismuth (Bi^{3+}) that resulted in the formation of a completely miscible solid solution, $MA_3(Sb_{1-x}Bi_x)_2I_9$ ($0 \leq x \leq 1$), of the parent components $MA_3Sb_2I_9$ and $MA_3Bi_2I_9$. Composition dependence of the optical bandgap in such $MA_3(Sb_{1-x}Bi_x)_2I_9$ solid state alloys showed evidence of a quadratic nature (bowing) where an intermediate compound containing equimolar contribution of antimony and bismuth ($MA_3(Sb_{0.5}Bi_{0.5})_2I_9$) offered the narrowest bandgap of around 1.90 eV; markedly lower than the bandgap of the end members $MA_3Sb_2I_9$ (2.36 eV) and $MA_3Bi_2I_9$ (2.16 eV). Evolution of the band edges in the materials was probed through scanning tunneling spectroscopy (STS) and the respective variation of transport gap also showed a bow-like behavior that was predominantly governed by the movement of conduction band edge. The mechanism behind this phenomenon could be due to an interplay between spin-orbit coupling and structural modifications induced by the isovalent substitution, although calculations would be required to corroborate this. In concurrence to such bandgap bowing, power conversion efficiency of planar heterojunction solar cells based on $Cu:NiO/MA_3(Sb_{1-x}Bi_x)_2I_9/ZnO$ heterojunctions also showed a bowing effect with respect to the composition of the absorber layer. This work hence presents a systematic study on the bandgap bowing behavior in zero-dimensional $MA_3(Sb_{1-x}Bi_x)_2I_9$ solid state alloys.

2. Results and discussion

2.1 Characterization of $MA_3(Sb_{1-x}Bi_x)_2I_9$ solid state alloys

We have recorded optical absorption spectra of all $MA_3(Sb_{1-x}Bi_x)_2I_9$ solid state alloys in their thin-film form to study the composition dependence of the bandgap. In Figs. 1a and b, we have presented representative spectra normalized to a film thickness of 125 nm and their corresponding Tauc plots, respectively. The spectra of $MA_3Sb_2I_9$ and $MA_3Bi_2I_9$ showed their

characteristic peaks at around 466 and 505 nm, respectively, which matched with the reported results.[2,17] It is worth mentioning here that the absorption spectra of $MA_3Bi_2I_9$ is dependent on orientation of the crystals, indicating a strong charge carrier localization in the material.[18] In addition, the presence of a pronounced peak in the absorption spectrum indicates existence of excitons in $MA_3Bi_2I_9$.[18] In contrast, $MA_3Sb_2I_9$ did not show any such strong excitonic nature in its absorption spectrum, indicating a lower density of defect states in the material than its bismuth analogue.[10] The spectrum corresponding to the intermediate composition ($x = 0.5$) also did not show any strong excitonic nature, moreover, a clear red-shift of the absorption edge could be visible. A change in the bandgap upon bismuth substitution in $MA_3Sb_2I_9$ was accordingly evidenced in the respective Tauc plots, as presented in Fig. 1b. It should be noted that, unlike $MAPbI_3$, the organic group does not contribute to the bandgap of $MA_3B_2I_9$ compounds.[1]
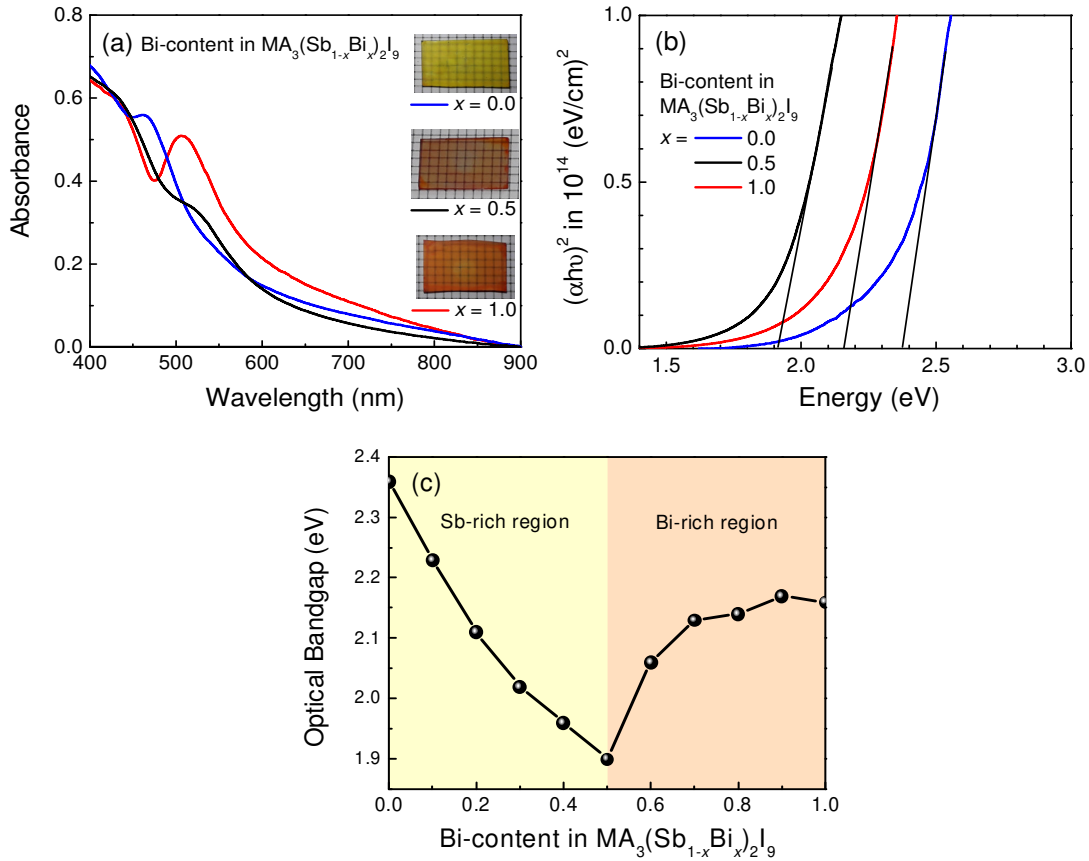

Fig. 1 (a) Optical absorption spectra and (b) corresponding Tauc plots of $MA_3(Sb_{1-x}Bi_x)_2I_9$ thin-films for a few representative values of x, and (c) compositional dependence of the optical bandgap in $MA_3(Sb_{1-x}Bi_x)_2I_9$ alloys. Inset of (a) shows photographs of representative $MA_3(Sb_{1-x}Bi_x)_2I_9$ thin-films.

When we studied the evolution of optical bandgap in $MA_3(Sb_{1-x}Bi_x)_2I_9$ ($0 \leq x \leq 1$) alloys with respect to the bismuth content (Fig. 1c), the variation of bandgap showed a nonmonotonic and nonlinear nature. Such a behavior could further be fitted by a quadratic expression and in solid state theory of semiconductor alloys, this phenomenon is commonly termed as 'bandgap bowing'.[19] As can be seen in the plot, the optical bandgap of $MA_3(Sb_{1-x}Bi_x)_2I_9$ alloys showed a steep red-shift from its initial value of 2.36 eV ($x = 0$, $MA_3Sb_2I_9$) to attain a minimum of 1.90 eV at an intermediate composition of $MA_3(Sb_{0.5}Bi_{0.5})_2I_9$ followed by a gradual and moderate blue-shift that saturates at 2.16 eV in $MA_3Bi_2I_9$. Therefore, the optical bandgap of composites over a range of antimony-bismuth combinations has lower value as compared to the end members of the series. Such a change in the bandgap has also resulted in a change in the color of the films. As shown in the inset of Fig. 1a, color of the films gradually changed from bright yellow in $MA_3Sb_2I_9$ to a dark orange in $MA_3(Sb_{0.5}Bi_{0.5})_2I_9$ and finally, to a bright orange in $MA_3Bi_2I_9$ with an increase in bismuth-content.

We then aimed to carry out a detailed study on the composition dependence of the bandgap. As such, for any binary composition of semiconductors, the lattice parameter of the resultant alloys can be estimated from Vegard's law. According to this empirical rule, the lattice parameter of an alloy between two semiconductors is approximately equal to the rule of mixtures (linear relationship) of the two constituents' lattice parameters at the same temperature. In many binary semiconducting systems, the bandgap is approximately a linear function of the lattice parameter and therefore Vegard's law can be generalized to a linear relationship between the bandgap and composition also.

$$E_g(x) = (1-x)E_{g|(x=0)} + xE_{g|(x=1)} \tag{1}$$

where, $E_g(x)$ is the bandgap of the composite with dopant content 'x' and $E_{g|(x=0)}$ and $E_{g|(x=1)}$ are bandgaps of the two end members of the family.

On the other hand, if the variation of bandgap with composition cannot be portrayed by a linear interpolation between band energies, a quadratic curvature correction term is usually incorporated on the right hand side of Eq.(1).[20] With such an additional term, the equation can be represented as:

$$E_g(x) = (1-x)E_{g|(x=0)} + xE_{g|(x=1)} - bx(1-x) \tag{2}$$

where, b is the bowing coefficient that accounts for a deviation from the linearity, $\Delta E_g(x) = bx(1-x)$. The magnitude and nature of this bowing coefficient usually plays a significant role in determining the origin of such a bandgap bowing in the intermediate compositions.

Since, in general, bandgap of a semiconductor alloy under the effect of bowing is smaller than the value estimated from the linear interpolation between the bandgaps of the end members; the bowing coefficient b is a positive quantity.[21] Typically, if b is small (a fraction of an electronvolt) and independent of composition, the bowing in most cases can be explained by the structural disorder effect.[22] This means that, in such materials, inclusion of a foreign element leads to a modification of the host crystal structure introducing strain in the host lattice. Such strains modify the lattice parameters and in turn tune the bandgap. On the contrary, if the bowing coefficient becomes large or composition-dependent (for example, $GaAs_{1-x}N_x$ alloys possess a b value of ~16 eV), the origin of bandgap bowing is usually more complex to explain through a single phenomenon.[23] Likewise, in case of $MA_3(Sb_{1-x}Bi_x)_2I_9$ solid solution, the variation in the bandgap with metal-composition cannot be explained by a single bowing coefficient. A rough estimate using Eq. (2) shows that while the value of the coefficient b in the antimony-rich region maintains almost a constant value which is larger than the value of the coefficient in the bismuth-rich region, the coefficient decreases sharply to a small value (a fraction of an electronvolt) with an increase in the bismuth content showing its composition dependent nature (Fig. 2). The overall value of b is close to the average of b in the two regions. The origin of bandgap bowing in $MA_3(Sb_{1-x}Bi_x)_2I_9$ cannot be explained by a constant, composition independent, single bowing coefficient; instead, it can be divided into a couple of regions, each having its own dominance in the bandgap trend. Hence, replacing the constant bowing coefficient (b) in Eq. (2) with a composition-dependent one (b'), the bandgap versus composition relationship can be modified as:

$$E_g = (1-x)E_{g|(x=0)} + xE_{g|(x=1)} - b'x(1-x) \text{ where } b' = b(x) \tag{3}$$
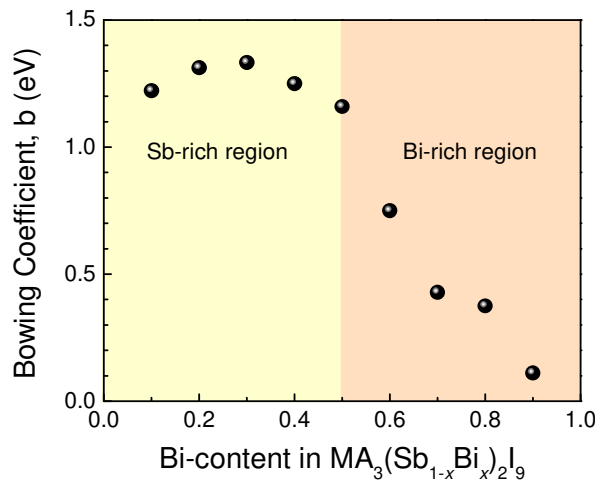

Fig. 2 Composition dependence of bowing coefficient.

As a structural change also plays a crucial role in the occurrence of bandgap bowing, we also studied the crystal structure of the $MA_3(Sb_{1-x}Bi_x)_2I_9$ thin-films. In this regard, we first of all aimed to achieve an insight into their structural stability by estimating the Goldschmidt's tolerance factor (t) which is defined as:[13]

$$t = \frac{(R_A + R_X)}{\sqrt{2}(R_B + R_X)} \qquad (4)$$

where, R_A, R_B, and R_X are the effective ionic radii of A- and B-site cations and X-site anion, respectively. Following such an empirical formula and considering the radii of MA^+ ($R_A =$ 180 pm), Sb^{3+} ($R_B = 76$ pm), Bi^{3+} ($R_B = 103$ pm), and I^- ($R_X = 220$ pm),[24] the tolerance factor values for $MA_3Sb_2I_9$, $MA_3(Bi_{0.5}Sb_{0.5})_2I_9$, and $MA_3Bi_2I_9$ compounds came out to be 0.96, 0.92, and 0.88, respectively. Typically, a large tolerance factor value signifies a low formation energy which in turn addresses a thermodynamically favorable and stable phase.[13] Hence our estimation indicated formation of a more stable structure with antimony at the B-site. We may mention here that it is customary to consider average effective ionic radius of Sb^{3+} and Bi^{3+} ($R_B = 89.5$ pm) while calculating tolerance factor in the substituted system, that is in the $MA_3(Sb_{0.5}Bi_{0.5})_2I_9$ composite.[12]

The structural characterizations were then carried out through X-ray diffraction (XRD) studies and the respective patterns are presented in Figs. 3a and b. Typically, the two end-members, namely $MA_3Sb_2I_9$ and $MA_3Bi_2I_9$, crystallize in a zero-dimensional (0 D) dimer-like structure with hexagonal symmetry ($P6_3/mmc$).[2,18] The crystals are formed with isolated bioctahedral face-sharing $(B_2I_9)^{3-}$ clusters separated by MA^+ groups; the clusters are analogous to quantum dots separated by ligands at the atomic level.[25] The XRD patterns of $MA_3Sb_2I_9$ thin-films showed the most intense peak at around 25° indicating a strong preferential growth along the (003) plane, $i.e.$, the c-axis of the crystal. Such a pattern is in well-agreement with the reported results for solution-processed $MA_3Sb_2I_9$ films;[2,11] only the peaks that could be indexed to $P6_3/mmc$ were present in the diffraction pattern ensuring phase purity of the material. XRD patterns of the other end-member, namely $MA_3Bi_2I_9$, also had a hexagonal symmetry and preferred growth along the (006) plane.[26] The XRD patterns thus revealed a strong orientation of both the end-members in the [001] direction. This phase-invariance of the end-members further strengthen the occurrence of bandgap bowing in the $MA_3(Sb_{1-x}Bi_x)_2I_9$ alloys as a quadratic evolution of the bandgap instead of two overlapping, linear, and Vegard-like behavior. XRD patterns of the intermediate compounds also showed a high preferential orientation of the crystallites along the same direction.
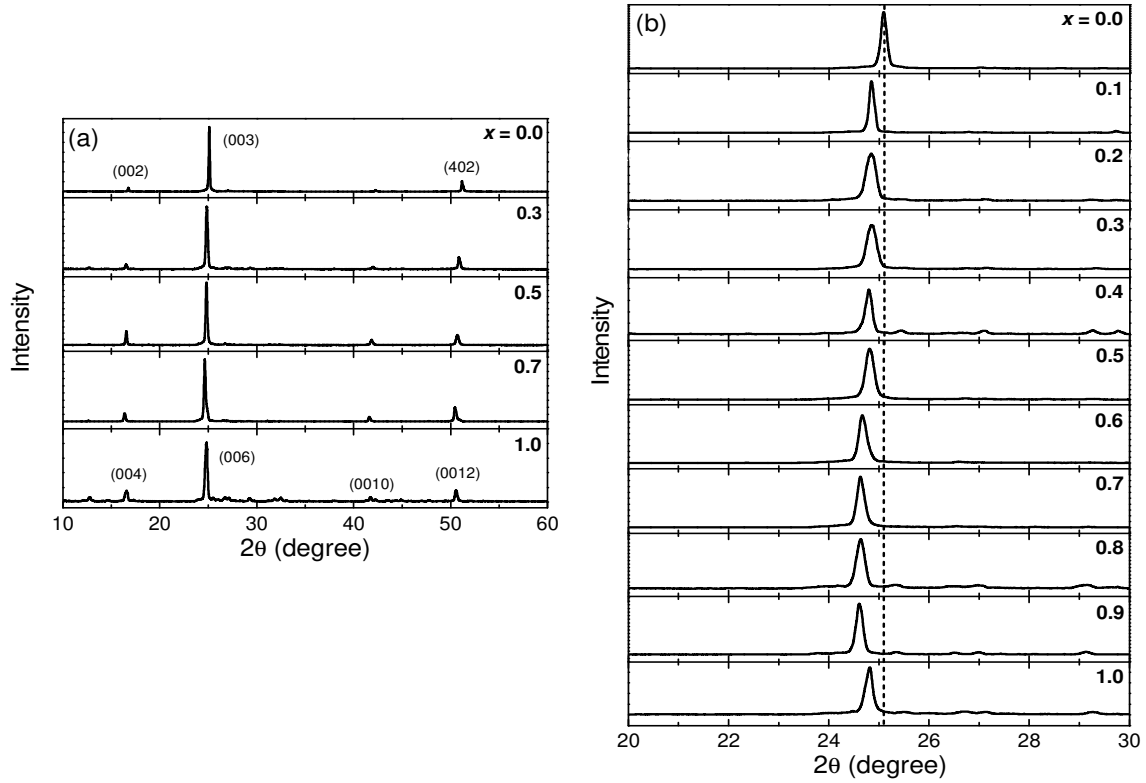
Fig. 3 XRD patterns of (a) $MA_3(Sb_{1-x}Bi_x)_2I_9$ thin-films with a few x values as mentioned in the legends and (b) zoomed view of the characteristic peak at ~25° for $MA_3(Sb_{1-x}Bi_x)_2I_9$ ($0 \leq x \leq 1$) compounds.

It is apparent that the hexagonal symmetry of $MA_3Sb_2I_9$ and $MA_3Bi_2I_9$ is retained in $MA_3(Sb_{1-x}Bi_x)_2I_9$ solid state alloys. A closer inspection of the signature peak at ~25° revealed a dopant-induced shift in the peak position implying a change in the lattice parameter (Fig. 3b). It may be recalled that in their trivalent cation form, bismuth has a larger effective ionic radius than that of antimony. Tensile strains are hence expected to form in $MA_3(Sb_{1-x}Bi_x)_2I_9$ compounds upon bismuth-incorporation. As a result, introduction of bismuth enlarged the d-spacing in the composite and shifted the characteristic peak towards the smaller angle. It also appears from the patterns that the tensile strain may have saturated in $MA_3Bi_2I_9$.

The XRD patterns were fitted using Pawley refinement to evaluate the lattice parameters of $MA_3(Sb_{1-x}Bi_x)_2I_9$ ($0 \leq x \leq 1$) solid state alloys and the respective values have been collated in Table S1†. Considering the preferred orientation of the materials along c-axis, we have studied evolution of the respective lattice parameter (c) and unit cell volume with bismuth content in the composites (Figs. 4a and b). As can be seen from Fig. 4a, with increasing bismuth content, the c-parameter increased from a value of 21.458(2) Å, for pristine $MA_3Sb_2I_9$ ($x = 0$), to 21.737(1) Å for $MA_3Bi_2I_9$ ($x = 1$) owing to a larger effective

ionic radius of Bi^{3+} as compared to Sb^{3+}. As a result of the increase in the c-parameter, volume of the unit cell also expanded continuously indicating an increase in unit cell parameters in $MA_3Sb_2I_9$ crystals upon bismuth substitution (Fig. 4b).
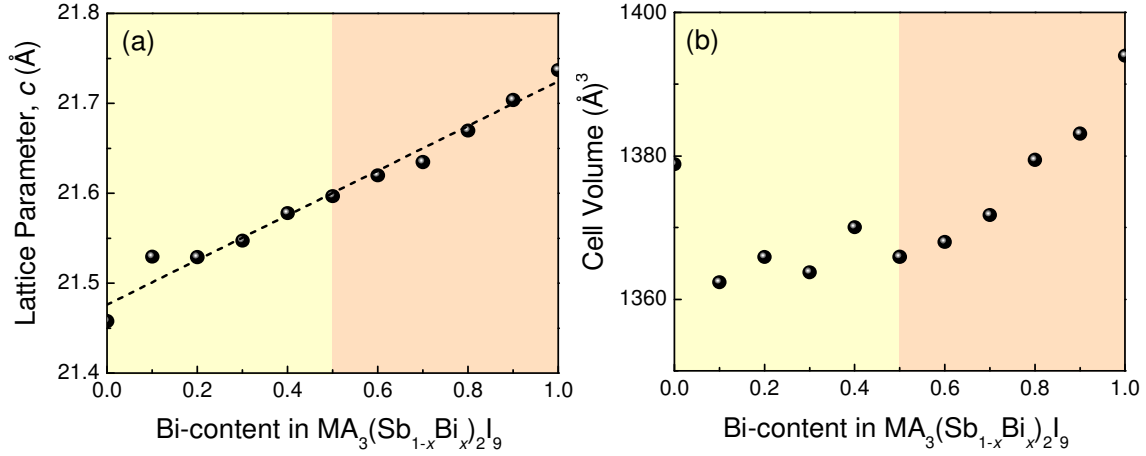

Fig. 4 Variation of (a) lattice parameter, c and (b) unit cell volume as a function of bismuth content in $MA_3(Sb_{1-x}Bi_x)_2I_9$ thin-films.

As evidenced from our characterizations, despite forming a completely miscible and compositionally homogeneous solid solution, alloys of $MA_3Sb_2I_9$ and $MA_3Bi_2I_9$ exhibited an unusual bandgap bowing behavior. The phenomena of bandgap bowing is typically observed in disordered II-VI and III-V semiconductor alloys and recently has been reported in halide perovskites $(MA(Sn_{1-x}Pb_x)I_3)$ as well.[16,21,23] Unlike the inorganic alloys, the underline mechanism of bandgap bowing in hybrid perovskite alloys is not clearly known yet and has been proposed so far as a competing effect between spin-orbit coupling (SOC) and lattice distortion.[16] As such, in the absence of a SOC effect, the optical bandgap of an alloy increases upon addition of an element having a higher effective ionic radius and the increase is expected to be linear following Vegard's law.[27] On the other hand, as observed in $MA(Sn_{1-x}Pb_x)I_3$ solid solution, inclusion of lead in $MASnI_3$ introduces SOC in the system due to high atomic number (Z) of lead and thereby lowers the bandgap of the alloys with increasing lead-content (x).[16] At higher value of x, lattice distortion causes an increase in the bandgap overpowering the effect of SOC. Here the lattice distortion appears in the system due to a higher effective ionic radius (r_{ion}) of lead(II) as compared to that of tin(II) (r_{ion} of Sn^{2+} and Pb^{2+} are 110 and 119 pm, respectively).[16] This causes a change in the crystal symmetry and geometry of the structure resulting in a phase transition from $P4mm$ space group (α phase) of tin-rich compositions, to $I4cm$ space group (β phase), of the lead-rich compositions.[16]

Based on the analysis of bandgap bowing in $MASn_{1-x}Pb_xI_3$, we speculate that SOC interactions would also appear in $MA_3(Sb_{1-x}Bi_x)_2I_9$ with the introduction of a high-Z element (bismuth) replacing antimony and would cause a bandgap reduction with an increase in the bismuth-content (x) in the system. Since, the effect of SOC is proportional to the fourth power of the atomic number of an element, we observed a sharp and linear red-shift of the bandgap with increasing bismuth-content in $MA_3(Sb_{1-x}Bi_x)_2I_9$ composition till $x \leq 0.5$ (Fig. 1c). On the other hand, as observed from our XRD studies, the introduction of bismuth in such metal-substituted perovskite derivatives led to structural modifications (expansion of unit cell volume) due to the significant difference in effective ionic radii of Sb^{3+} and Bi^{3+} (Fig. 4b); the latter having a larger ionic-radius, such structural change would widen the bandgap. We can therefore propose that like $MA(Sn_{1-x}Pb_x)I_3$, a competing effect of SOC and lattice strain existed in $MA_3(Sb_{1-x}Bi_x)_2I_9$ solid state alloys and has resulted in the observed bandgap bowing. We expect that SOC effects dominate in antimony-rich compositions ($x \leq$ 0.5) leading to a gradual lowering of bandgap and lattice distortion overpowered the proposed SOC effect in the bismuth rich compositions ($0.5 < x \leq 1.0$) causing an increase in the bandgap. Further work, in particular theoretical calculations, should be done to corroborate the influence of SOC in this system.

2.2 Scanning tunneling spectroscopy: density of states and band edges

Though detailed electronic structure calculations are required to completely understand this anomalous bandgap bowing behavior in $MA_3(Sb_{1-x}Bi_x)_2I_9$ perovskite derivatives, we aimed to get an insight to this phenomenon from scanning tunneling spectroscopy (STS). To do so, we recorded tunneling current with respect to an applied voltage for all the compositions and calculated the differential tunnel conductance (dI/dV) that has a correspondence to the density of states (DOS) of the materials. During STS measurements, since the bias was applied to the tip with respect to the substrate, the conduction band (CB) and valence band (VB) edges could be identified in the form of first peaks in the dI/dV spectra appearing in the negative and positive tip voltages respectively, with Fermi energy (E_F) being aligned to zero voltage (Fig. S1a†).[28] The localized nature of the STS measurements was taken into account by recording tunneling current from a large number of points on each of the ultrathin films; with the CB and VB edges estimated from each measurement being collated in the form of histograms (Fig. S1b†), the band edge energies of $MA_3(Sb_{1-x}Bi_x)_2I_9$ have been depicted in Fig. 5a and enlisted in Table S2†.
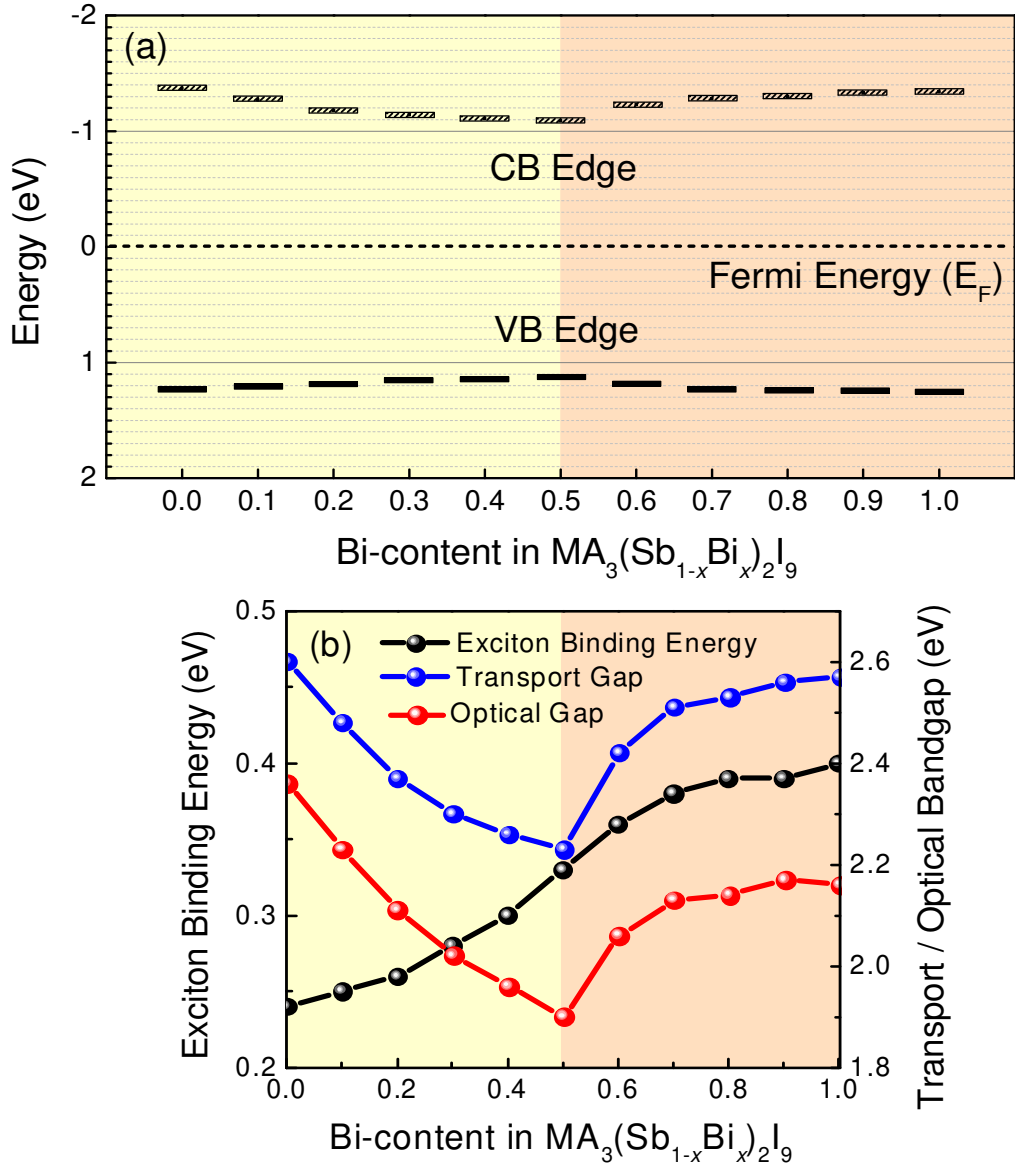
Fig. 5 (a) CB and VB-edges as obtained from STS and (b) variation of transport gap, optical bandgap, and exciton binding energy in $MA_3(Sb_{1-x}Bi_x)_2I_9$ thin-films as a function of bismuth content (x).

After determination of the band-edges, we estimated the transport gap in each of the $MA_3(Sb_{1-x}Bi_x)_2I_9$ alloys (Table S2†). Similar to the optical bandgap, variation of the transport gap also showed a bowing effect with the gap of the $MA_3(Sb_{1-x}Bi_x)_2I_9$ alloys being smaller than those of the end members. For each of the materials, the transport gap derived from STS studies was found to be wider than the corresponding optical bandgap and the difference in energy can be attributed to the exciton binding energy of the semiconductor.[29] Although both transport gap and optical bandgap in $MA_3(Sb_{1-x}Bi_x)_2I_9$ exhibited the bowing effect with composition, their difference or exciton binding energy shows a monotonic increment with

addition of bismuth in the system (Fig. 5b). As stated earlier, the exciton binding energy of $MA_3Sb_2I_9$ is known to be less than that in $MA_3Bi_2I_9$ due to a smaller spatial restriction and also a dielectric mismatch between the organic and inorganic layers.[1] Hence, the trend obtained from our STS measurements was in agreement with the reported results.

If we consider the movement of the band edges during such an anomalous bandgap behavior, it can be seen that the shift of the CB-edge with composition has played a dominant role in the evolution of transport gap. Movement of the VB-edge, conversely, was noticeable but marginal. Such a behavior can be understood by considering the composition of band edges in such lead-free hybrid perovskite derivatives. Since, both antimony and bismuth, in their trivalent form, have similar electronic configurations (ns^2) to bivalent lead; the composition of band edges in these perovskite derivatives is similar to the archetypical $MAPbI_3$ perovskite.[30] Hence, in $MA_3B_2I_9$ compounds, the VB-edge is composed of iodine p (I $5p$) with metal s (Sb $5s$ or Bi $6s$) orbitals whereas the CB-edge is predominantly composed of metal p (Sb $5p$ or Bi $6p$) orbitals, respectively, and they are confined zero-dimensionally in the $(B_2I_9)^{3-}$ bioctahedra where B = Sb or Bi.[26] In accordance to such a band structure, the freshly introduced energy states of bismuth modulated the CB-edge of the $MA_3(Sb_{1-x}Bi_x)_2I_9$ more than the VB-edge and in bismuth rich compositions, movement of both the edges away from the Fermi energy widened the bandgap. Such an evolution of the band-edge energies also nullifies the possibility of band inversion behind the bowing phenomenon. Goyal *et al.* proposed that bandgap bowing in $MASn_{1-x}Pb_xI_3$ solid solution originates due to charge separation in the band-edges of the alloys.[15] They argued that in all such alloys, the VB-edge inherits its character from Sn s/I p combination whereas the CB-edge is derived from Pb p/I p combination. The differences in the energies of Pb and Sn s and p orbitals eventually lead to a lower bandgap in the intermediates compared to the pure end members. However, if such a scenario is dominant in the bandgap bowing of $MA_3(Sb_{1-x}Bi_x)_2I_9$ alloys, movement of the band-edges away from the Fermi energy after reaching their closest position cannot be justified. Since, we have observed a bow-like evolution of the band-edges as well with respect to the composition of the alloys, it rules out the possibility of bandgap bowing due to band inversion. Besides locating the band-edges, information on the type of conductivity can also be gathered from STS measurements and corresponding DOS spectra. Typically, the $MA_3B_2I_9$ perovskite derivatives processed through a solution-based approach have been reported to have p-type conductivity due to presence of intrinsic acceptor type defects.[26] Our STS results show that the VB-edge in $MA_3Sb_2I_9$ is slightly closer to E_F as compared to CB-edge inferring its p-type nature. Due to the isovalent nature of substitution in $MA_3(Sb_{1-}$

$_x$Bi$_x$)$_2$I$_9$, the nature of conductivity was found to be unaffected over the entire range of bismuth-content; however its strength was stronger in bismuth-rich systems possibly due to a higher concentration of defects.

The non-monotonic evolution of bandgap in MA$_3$(Sb$_{1-x}$Bi$_x$)$_2$I$_9$ alloys is in contrast to the bandgap-tailoring in bismuth-doped MAPbBr$_3$ crystals. Being a heterovalent dopant in the MAPbBr$_3$ structure, bismuth led to a change in the type of conductivity; due to the presence of impurity energy levels within the bandgap of the host perovskite, such doping also resulted in bandgap narrowing in bismuth-doped MAPbBr$_3$.[31] However, in these alloys, the quadratic dependence of bandgap on bismuth-content cannot be attributed to such defect-induced bandgap tailoring. Moreover, since defects states also contribute to tunneling current, presence of defects influences the distribution of band-edge energies. As presented in Fig. S1b†, the FWHM of energy-histograms, which implies the distribution of band-energies, was quite narrow and showed a little or no change with an increase in bismuth-content. Therefore, we can infer that the defect-states induced by bismuth-doping do not play a prime role in the bandgap bowing of MA$_3$(Sb$_{1-x}$Bi$_x$)$_2$I$_9$ alloys.

It has been proposed that the crystal potential in solid-state alloys varies aperiodically due to random variations in occupation of its metal sites by parent elements and this give rise to the bandgap bowing phenomenon.[32] This non-linear, quadratic to be specific, dependence of bandgap on the composition of the alloys can be attributed to the fundamental difference in electronic structure between the parent compounds, namely MA$_3$Sb$_2$I$_9$ and MA$_3$Bi$_2$I$_9$, resulting in a significant modification in the band structure of the former upon alloying with the latter.

As STS measurements have the ability to probe the local density of states (LDOS) of a semiconductor with a high spatial and energetic resolution, band energies obtained from STS studies refer to energy levels as "seen" by charge carriers in devices.[28] We hence aimed to visualize the tentative band-alignment of MA$_3$(Sb$_{1-x}$Bi$_x$)$_2$I$_9$ ($0 \leq x \leq 1$) with Cu:NiO and ZnO as carrier-selective contacts. As presented in Fig. 6, the band edges of representative compositions with x = 0.0, 0.5 and 1.0 formed type-II band-alignments both at Cu:NiO/MA$_3$(Sb$_{1-x}$Bi$_x$)$_2$I$_9$ and MA$_3$(Bi$_{1-x}$Sb$_x$)$_2$I$_9$/ZnO interfaces ensuring hindrance free carrier transport in the devices for all the compositions.

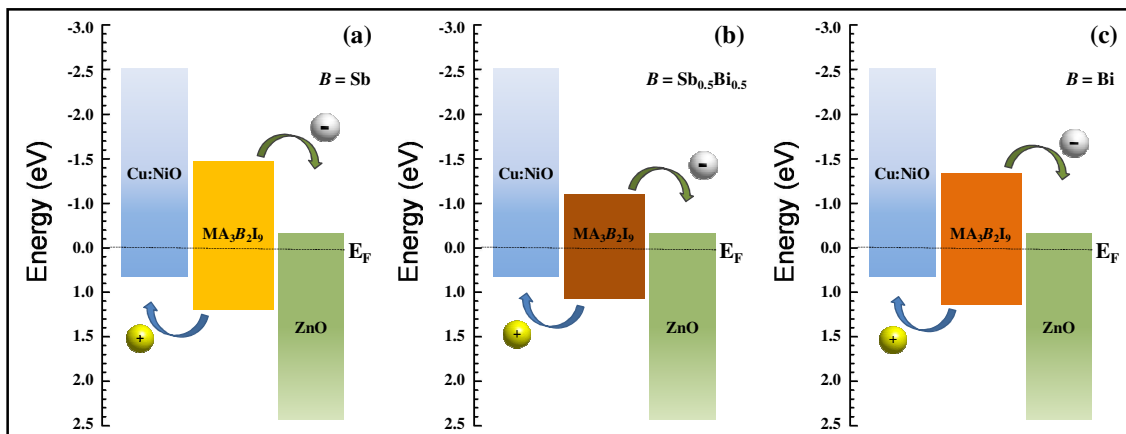**Fig. 6** Schematic energy-level diagrams of (a) Cu:NiO/MA$_3$Sb$_2$I$_9$/ZnO, (b) Cu:NiO/MA$_3$(Sb$_{0.5}$Bi$_{0.5}$)$_2$I$_9$/ZnO and (c) Cu:NiO/MA$_3$Bi$_2$I$_9$/ZnO heterojunctions. The dotted line presents Fermi energy (E$_F$) after contact.

2.3 Surface morphological and compositional studies

Morphology has been a long standing roadblock for solution-processed lead-free hybrid halide materials in achieving a promising photovoltaic performance.[33,34] Due to the use of a single precursor based solution-approach during fabrication, MA$_3$$B$$_2I_9$ and its derivatives are prone to form inhomogeneous films with incomplete coverage.[10] An anti-solvent treatment during the fabrication of the films however addresses this concern to some extent by controlling the homogeneity and surface morphology of the films.[11] Between the two commonly used anti-solvents, namely toluene and chlorobenzene, toluene promotes amorphous nature in the material.[10] Hence, we intentionally refrained from its use and chose the latter. Images of films having representative bismuth-contents before and after anti-solvent treatment were recorded with scanning electron microscope (SEM) and have been placed in Fig. S2†. It can be clearly observed from the comparison that the untreated films contained irregular-shaped crystals along with an extremely rough surface-morphology and incomplete substrate-coverage. Both parameters improve significantly after chlorobenzene treatment. The morphology of the treated films showed presence of hexagon-shaped crystals with micron-sized grains further ensuring a hexagonal crystal structure in these materials. It may be restated here that such a structure has already been confirmed from XRD studies.
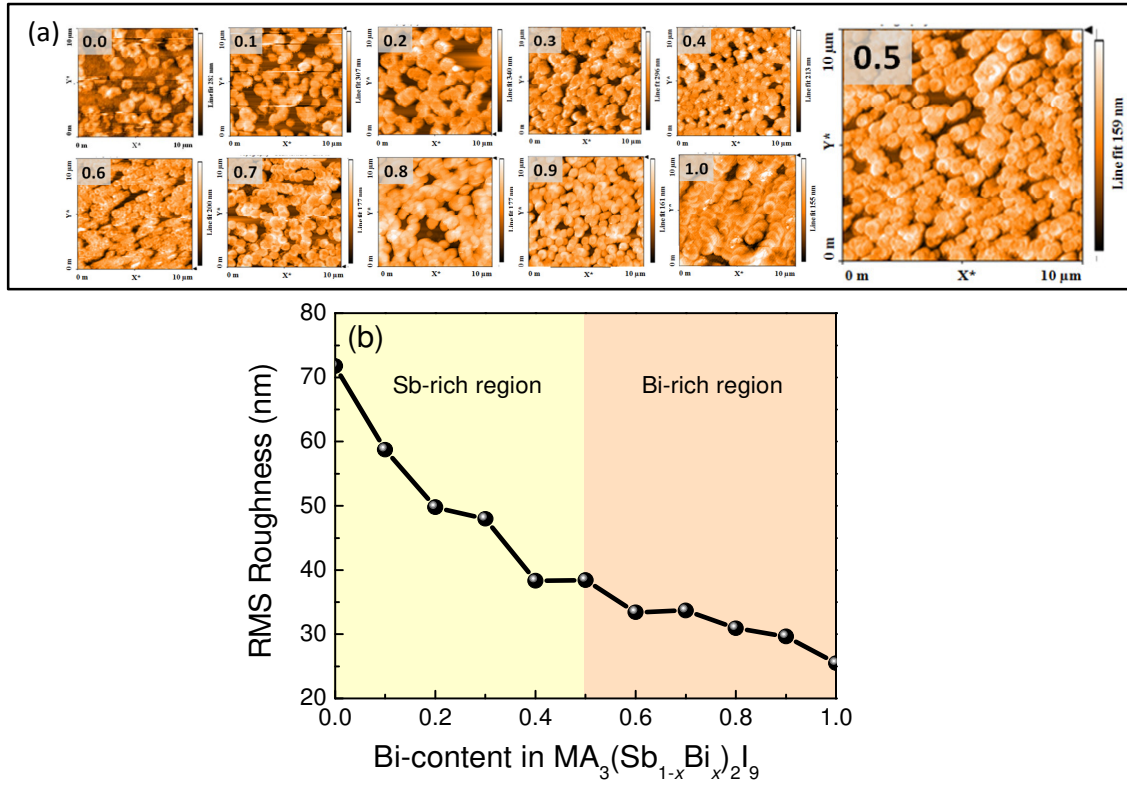
Fig. 7 (a) AFM topographies of $MA_3(Sb_{1-x}Bi_x)_2I_9$ thin-films having different bismuth-content and (b) variation of RMS roughness with bismuth-content in $MA_3(Sb_{1-x}Bi_x)_2I_9$ thin-films.

We then proceeded to study the influence of bismuth-incorporation on the surface morphology of $MA_3(Sb_{1-x}Bi_x)_2I_9$ films. Typical two-dimensional (2D) topographies of thin-films respective to each composition were recorded with atomic force microscope (AFM) and have been shown in Fig. 7a. The images showed formation of hexagonal crystals of comparable sizes over the entire range of bismuth-substitution.[10,35] A closer inspection of each film however showed an island growth, *i.e.* presence of small clusters of hexagons, on the films leading to formation of an uneven surface-texture. The root-mean square (RMS) surface roughness of the films was calculated in the area of $10{\times}10$ μm^2, by using the equipment's routine software. As evidenced from such estimation, uniformity of the films could be seen to relatively improve with increasing bismuth-content in $MA_3(Sb_{1-x}Bi_x)_2I_9$ (Fig. 7b). This indicates a relative improvement of grain size in the films formed with bismuth-rich compositions. The high surface roughness associated with all the $MA_3(Sb_{1-x}Bi_x)_2I_9$ thin-films inferred an inherently non-uniform morphology of the films irrespective of the composition. Essentially, such an inhomogeneous nature is involved in the solution-based fabrication

procedure of the films and a gaseous-phase deposition technique such as chemical vapor deposition could be used to achieve a better control on morphology and uniformity.[36]

To study the stoichiometry of the films, we carried out a quantitative compositional analysis through energy dispersive X-ray (EDX) measurement. Due to a non-uniform morphology of the films and localized nature of EDX measurement, we carried out EDX analysis at several locations on the films including both on the hexagons and the surface and also in films formed in different batches. Fig. S2b† shows the typical SEM images for the three representative compositions x = 0.0, 0.5 and 1.0 of $MA_3(Sb_{1-x}Bi_x)_2I_9$ binary alloys where the points of EDX measurements have been marked with yellow dots. In Fig. S3† EDX patterns of the intermediate compound with x = 0.5 have been presented whereas the detailed relative analysis for all the three composites has been appended in Table S3†. As can be seen from the compositional studies, hexagons in all the films expectedly showed a clear presence of the metal (antimony or bismuth or both) and iodine; in all cases, the antimony-to-bismuth ratio was close to the stoichiometry used during the material formation inferring compositional homogeneity and reproducibility of the as-prepared perovskite thin-films. However, the iodine-to-metal ratio was found to be less than the stoichiometry that can ascribed to the inherent limitations and poor reproducibility of EDX in quantifying iodine.[37] Interestingly, the uniform regions also showed presence of metal and iodine indicating existence of a thin-layer of $MA_3(Sb_{1-x}Bi_x)_2I_9$ covering the substrate. Thus, from EDX analysis, we could infer that the films were free of pin-holes and suitable to study their photovoltaic properties.

2.4 Photovoltaic characteristics

To study the influence of bandgap bowing on photovoltaic properties of $MA_3(Sb_{1-x}Bi_x)_2I_9$ binary perovskite derivatives, we fabricated and characterized planar heterojunction devices having an inverted geometry. In such devices, the $MA_3(Sb_{1-x}Bi_x)_2I_9$ layer was sandwiched between Cu:NiO and ZnO hole- and electron-selective contacts, respectively. In Fig. 8a, we have presented *I-V* characteristics of devices based on some of the compositions, namely x = 0.0. 0.5, and 1.0, that is $MA_3Sb_2I_9$, $MA_3(Sb_{0.5}Bi_{0.5})_2I_9$, and $MA_3Bi_2I_9$ under dark and 1 sun illuminated conditions. With *I-V*s of all the devices under 1 sun being collated in Fig. S4†, variation of power conversion efficiency (PCE) and short-circuit current density (J_{SC}) with bismuth-content (x) has been presented in Fig. 8b. The respective photovoltaic parameters of all deviceshave been summed up in Table 1. From the characteristics, J_{SC} of the devices could be seen to increase continuously from 2.76 mA/cm^2 for $MA_3Sb_2I_9$ (x = 0) based devices to a

maximum value of 3.58 mA/cm^2 with materials having an intermediate content of bismuth. With bismuth-rich compositions, the J_{SC} value of the devices decreased; that is, the J_{SC} also showed a bowing-nature in accordance to the bandgap dependence of the materials and the highest J_{SC} was yielded for the lowest bandgap material.
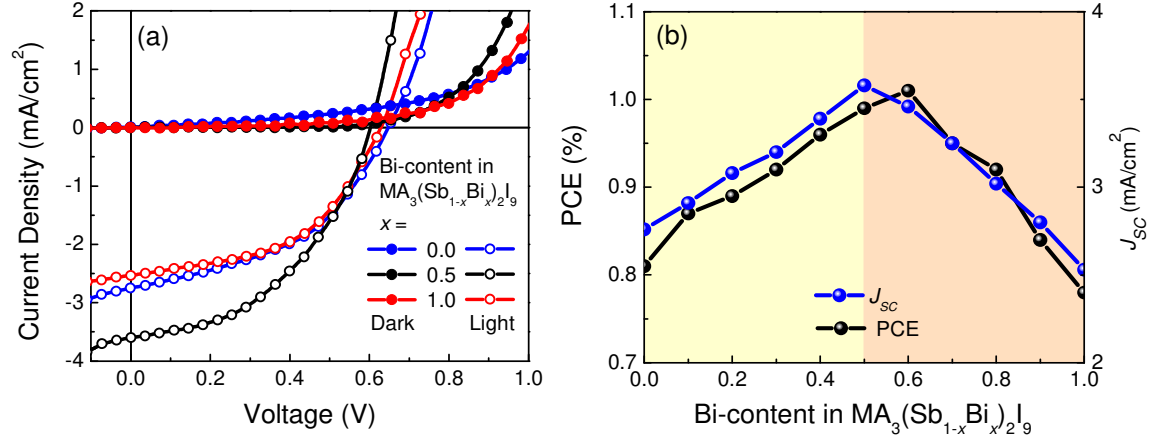

Fig. 8 (a) *I-V* characteristics of Cu:NiO/MA$_3$(Sb$_{1-x}$Bi$_x$)$_2$I$_9$/ZnO heterojunction devices under dark and illuminated conditions for x = 0.0, 0.5, and 1.0 and (b) variation of PCE and J_{SC} with bismuth-content in the material.

In general, V_{OC} in perovskite solar cells is governed by the energy-difference between CB-edge of the perovskite layer and VB-edge of the hole-selective contact.[38] As found in the STS measurements and respective density of states (DOS) spectra, introduction of Bi^{3+} in MA$_3$Sb$_2$I$_9$ structure specially influenced the CB-edge, and accordingly modulated the V_{OC} value of the devices. Considering the wide bandgap of MA$_3$$B_2I_9$ perovskite derivatives, the reported V_{OC} values are still low indicating a high V_{OC}-loss in the devices due to both large exciton binding energy of the materials and significant degree of carrier recombination in the devices.[2,18,35] The low V_{OC} in our devices can be similarly explained.

While an estimation of exciton binding energy has already been made from transport gap and optical bandgap measurements (Fig. 5b), the fill-factor in solar cells is indicative of the recombination phenomena in the devices. Although, the fill-factor of the devices improved upon bismuth substitution, the generally low values (Table 1) signify a high degree of trap-assisted recombination in the devices.

Table 1 Photovoltaic parameters of Cu:NiO/MA$_3$(Sb$_{1-x}$Bi$_x$)$_2$I$_9$/ZnO heterojunction devices with bismuth-content (x).

Bi-content (x)	J_{SC} (mA/cm^2)	V_{OC} (V)	FF (%)	PCE (%)
0.0	2.76	0.65	0.45	0.81
0.1	2.91	0.65	0.46	0.87
0.2	3.08	0.63	0.46	0.89
0.3	3.20	0.60	0.47	0.90
0.4	3.39	0.59	0.48	0.96
0.5	3.58	0.58	0.48	0.99
0.6	3.46	0.60	0.49	1.01
0.7	3.25	0.60	0.49	0.95
0.8	3.02	0.61	0.50	0.92
0.9	2.80	0.61	0.49	0.84
1.0	2.53	0.62	0.50	0.78

As a cumulative effect of all the parameters, the PCE of the devices was optimized to a value of ~1% at x = 0.6. The value is superior to devices with both the end-members, namely MA$_3$Sb$_2$I$_9$ (PCE = 0.81%) and MA$_3$Bi$_2$I$_9$ (PCE = 0.78%). An optimum balance between the bandgap, surface roughness, and exciton binding energy in MA$_3$(Sb$_{1-x}$Bi$_x$)$_2$I$_9$ with x = 0.6 composition can be the reason behind the feat. However, the observed PCE parameteris significantly lower than the standard MAPbI$_3$ perovskite solar cells that can be attributed to high effective masses of the carriers along the c-axis, poor surface morphology of these lead-free perovskite derivatives, and a non-optimal bandgap.[39]

3. Conclusions

In conclusion, we have systematically studied the effect of bismuth substitution in MA$_3$Sb$_2$I$_9$ perovskite-derivatives that evidenced a bowing behavior in the bandgap. Such a non-linear dependence of bandgap on the composition of MA$_3$(Sb$_{1-x}$Bi$_x$)$_2$I$_9$ solid solution led to the achievement of a bandgap of 1.90 eV at an intermediate composition (x = 0.5) which is lower than the bandgap of both the pure end-members MA$_3$Sb$_2$I$_9$ (2.36 eV, x = 0.0) and MA$_3$Bi$_2$I$_9$ (2.16 eV, x = 1.0). STS measurements and thereby DOS spectra, yielding CB and VB-edges of the compounds, has also evidenced the bowing phenomenon in the transport gap of MA$_3$(Sb$_{1-x}$Bi$_x$)$_2$I$_9$ solid state alloys. By estimating optical and transport gaps at different

compositions, we have derived exciton binding energies, which could be seen to increase continuously with increasing bismuth content. The bowing behavior in bandgap could be due to a combined effect of spin-orbit coupling (SOC) and structural modifications which were introduced to the $MA_3Sb_2I_9$ system due to inclusion of high-Z element bismuth. Calculations would however be required to confirm the role of SOC. The planar heterojunction (*p-i-n*) devices based on $MA_3(Sb_{1-x}Bi_x)_2I_9$ showed type-II band-alignment at the both interfaces with carrier-selective layers (namely *p-i* and *i-n*) and exhibited solar cell characteristics. Interestingly, performance of the devices, when plotted as a function of bismuth-content, exhibited dependence on the change in bandgap, morphology, and exciton binding energy and yielded a PCE of ~1% in these zero-dimensional lead-free hybrid halide perovskite derivatives.

4. Methods

4.1 Materials

Methylammonium iodide (CH_3NH_3I) was purchased from M/s Dyesol Australia Pty. Ltd. Antimony(III) iodide (98%; SbI_3), bismuth(III) iodide (99%; BiI_3), chlorobenzene (anhydrous, 99.8%), copper(II) chloride dihydrate (ACS reagent, ≥99.0%; $CuCl_2 \cdot 2H_2O$), diethanolamine (reagent grade, ≥98.0%; $HN(CH_2CH_2OH)_2$) nickel(II) acetate tetrahydrate (purum p.a., ≥99.0%; $Ni(OCOCH_3)_2 \cdot 4H_2O$), ethylene glycol (for analysis ≥ 99.5%; C_2H_5OH), methanol (for HPLC, ≥99.9%, CH_3OH) and N,N-dimethylformamide (anhydrous 99.8%; DMF) were purchased from Sigma-Aldrich, Inc. Zinc acetate dihydrate (extra pure, 99.5%; $Zn(OCOCH_3)_2 \cdot 2H_2O$) and potassium hydroxide pellets (extra pure, 85%, KOH) were purchased from Loba Chemie Pvt. Ltd. The materials, which were sensitive to moisture and ambient condition, were stored in a nitrogen filled glovebox to prevent degradation. All the chemicals were used without further purification or treatment.

4.2 Fabrication of $MA_3(Sb_{1-x}Bi_x)_2I_9$ thin-films

$MA_3(Sb_{1-x}Bi_x)_2I_9$ ($0 \leq x \leq 1$) thin-films were fabricated under ambient condition by following a reported solution-based single-precursor approach[40] assisted by an anti-solvent treatment.[11] Briefly, 0.4 M methylammonium iodide and 0.3 M metal iodide, namely BiI_3 and SbI_3 with a stoichiometric ratio between 0.0 – 1.0 in a step of 0.1, were mixed in 1 mL of anhydrous N,N-dimethylformamide (DMF) and stirred overnight at 70 °C in an ambient condition to form a precursor solution of vermilion color. The solution was then spun on to preconditioned substrates at 2500 rpm for 30 s; during the twelfth second of the coating, the films were washed with ~100 μL of warm (70 °C) chlorobenzene (HPLC-grade) for fast deposition crystallization (FDC) of the material. The films were then annealed at 100 °C for half an hour to complete the film formation and crystallization processes.

4.3 Fabrication of Cu:NiO thin-films and surface modified ZnO nanoparticles

The Cu:NiO thin-films and surface-modified ZnO nanoparticles were synthesized following reported solution based approaches.[41,42] For example, Cu:NiO thin-films were formed through a conventional sol-gel reaction route, where the sol was prepared by mixing 0.4 M nickel(II) acetate tetrahydrate with 5 at% copper(II) chloride (as dopant) in 10 mL methanol at room temperature. After complete dissolution of the materials, 0.8 mL of diethanolamine was added dropwise under stirring condition to prepare the gel. The precursor was then spun on the substrates and subsequently annealed at 425 °C in air to form the films.

ZnO nanoparticles, on the other hand, were grown by following a typical hydrolysis route. In brief, the zinc precursor solution was first prepared by dissolving 0.04 M zinc acetate dihydrate in 10 mL ethylene glycol at 80 °C until a homogeneous and transparent solution was obtained. To oxidize, a 0.04 M solution of KOH in 10 mL ethylene glycol was dropwise added into the solution of zinc until turbidity appears in the sol indicating formation of ZnO nanoparticles. The solution was then sonicated for 30 min followed by addition of 0.1 mL of oleic acid for surface modification of the as-prepared nanoparticles. They were then collected by centrifugation at 8000 rpm for 15 min, sifted through a syringe filter, and redispersed in chlorobenzene for further application.

4.4 Characterization of materials

The materials were characterized by UV−vis optical absorption spectroscopy and X-ray diffraction (XRD) studies. The measurements were carried out with a Shimadzu UV-2550 spectrophotometer and Rigaku MINIFLEX 600 X-Ray Diffractometer (Cu K$\alpha_{1,2}$ radiation), respectively. Surface morphology of the films was recorded with a Nanosurf Easyscan2 atomic force microscope (AFM) in non-contact mode and Jeol JSM-5600 scanning electron microscope (SEM). Compositional analyses of the materials were carried out from energy dispersive X-ray analysis (EDXA) using Oxford Inca EDX system attached to the SEM. The materials were further probed with a Nanosurf Easyscan2 scanning tunneling microscope (STM) in ambient conditions. From the tunneling current versus tip voltage characteristics, differential tunnel conductance (dI/dV) spectra that have a correspondence to density of states (DOS) of the materials were derived, enabling us to locate the conduction and valence band (CB and VB, respectively) edges of the semiconductors. Ultrathin-films required for characterization in an STM were formed on n-type silicon wafers (arsenic-doped) having a resistivity of 3−10 mΩ·cm as a substrate electrode. The films for STS measurements were cast at a higher speed (rpm) from the same stock solutions. During the measurements, voltage was applied to the tip, which was formed through a mechanical cut of a Pt/Ir (80:20) wire having a diameter of 0.25 mm. For approach of the tip, a bias of +2.0 V was applied through a feedback loop to achieve a set current of 1 nA.

4.5 Fabrication of devices

Solar cells were fabricated under an ambient condition. Indium tin oxide (ITO) coated glass substrates were first cleaned through a usual protocol followed by ultraviolet−ozone (UVO) treatment for 20 min. As an hole-transport layer (HTL), copper-doped nickel(II) oxide (Cu:NiO) thin-films were formed following the sol−gel reaction route. The process was repeated until a film-thickness of ∼40 nm was achieved. The HTL-coated substrates were then subjected to a preheating at 70 °C for 10 min. The perovskite layer (∼125 nm thick) was then formed following the process described above. As an electron-transport layer (ETL), ZnO was spun at 3000 rpm for 30 s from a chlorobenzene solution (20 mg/mL), followed by annealing at 100 °C for 20 min. Thickness of the ZnO layer was optimized to around 25 nm. To complete device fabrication process, substrates were then transferred to a vacuum chamber where aluminum strips, orthogonal to the ITO ones, were thermally evaporated to form top electrodes (100 nm thick). Active area of the cells was 10 mm^2.

4.6 Characterization of devices

Current−voltage (*I*−*V*) characteristics of the devices under dark and 1 sun illumination conditions were recorded with a Keithley 2636A electrometer using LabTracer software. The measurements were carried out under the inert environment of a glove box. Three-axis micropositioners having pressure-loaded spring probe contacts were used to connect the electrodes of the devices to the electrometer. A 300 W solar simulator (Newport-Oriel Sol3A) attached with an AM1.5 filter placed outside the glove box acted as a source for illumination through the transparent base of the glove box. While recording *I*−*V* characteristics under an illumination condition, regions outside the cell under probe were covered to avoid any possible contributions from neighboring areas or devices.

Conflict of Interest

The authors declare no conflict of interest.

References

1   B. W. Park, B. Philippe, X. L. Zhang, H. Rensmo, G. Boschloo and E. M. J. Johansson, *Adv. Mater.*, 2015, **27**, 6806-6813.

2   K. M. Boopathi, P. Karuppuswamy, A. Singh, C. Hanmandlu, L. Lin, S. A. Abbas, C. C. Chang, P. C. Wang, G. Li and C. W. Chu, *J. Mater. Chem. A*, 2017, **5**, 20843-20850.

3   M. I. Saidaminov, O. F. Mohammed and O. M. Bakr, *ACS Energy Lett.*, 2017, **2**, 889-896.

4   L. M. Wu, X. T. Wu and L. Chen, *Coord. Chem. Rev.*, 2009, **253**, 2787-2804.

5   M. H. Du, *J. Mater. Chem. A*, 2014, **2**, 9091-9098.

6   J. H. Chang, T. Doert and M. Ruck, *Z. Anorg. Allg. Chem.*, 2016, **642**, 736-748.

7   Z. Xiao, Z. Song and Y. Yan, 2019, **18**, 1803792

8   A. J. Lehner, D. H. Fabini, H. A. Evans, C. A. Hebert, S. R. Smock, J. Hu, H. B. Wang, J. W. Zwanziger, M. L. Chabinyc and R. Seshadri, *Chem. Mater.*, 2015, **27**, 7137-7148.

9   A. K. Baranwal, H. Masutani, H. Sugita, H. Kanda, S. Kanaya, N. Shibayama, Y. Sanehira, M. Ikegami, Y. Numata, K. Yamada, T. Miyasaka, T. Umeyama, H. Imahori and S. Ito, *Nano Converg.*, 2017, **4**, 26.

10 J. C. Hebig, I. Kuhn, J. Flohre and T. Kirchartz, *ACS Energy Lett.*, 2016, **1**, 309-314.

11 S. Chatterjee and A. J. Pal, *ACS Appl. Mater. Interfaces*, 2018, **10**, 35194-35205.

12 R. Nie, A. Mehta, B. W. Park, H. W. Kwon, J. Im and S. I. Seok, *J. Am. Chem. Soc.*, 2018, **140**, 872-875.

13 Z. Li, M. J. Yang, J. S. Park, S. H. Wei, J. J. Berry and K. Zhu, *Chem. Mater.*, 2016, **28**, 284-292.

14 F. Liu, C. Ding, Y. H. Zhang, T. S. Ripolles, T. Kamisaka, T. Toyoda, S. Hayase, T. Minemoto, K. Yoshino, S. Y. Dai, M. Yanagida, H. Noguchi and Q. Shen, *J. Am. Chem. Soc.*, 2017, **139**, 16708-16719.

15 A. Goyal, S. McKechnie, D. Pashov, W. Tumas, M. van Schilfgaarde and V. Stevanovic, *Chem. Mater.*, 2018, **30**, 3920-3928.

16 J. Im, C. C. Stoumpos, H. Jin, A. J. Freeman and M. G. Kanatzidis, *J. Phys. Chem. Lett.*, 2015, **6**, 3503-3509.

17 T. Singh, A. Kulkarni, M. Ikegami and T. Miyasaka, *ACS Appl. Mater. Interfaces*, 2016, **8**, 14542-14547.

18 M. Abulikemu, S. Ould-Chikh, X. H. Miao, E. Alarousu, B. Murali, G. O. N. Ndjawa, J. Barbe, A. El Labban, A. Amassiana and S. Del Gobbo, *J. Mater. Chem. A*, 2016, **4**, 12504-12515.

19 C. S. Schnohr, *Appl. Phys. Rev.*, 2015, **2**, UNSP 031304.

20 H. W. King, *J. Mater. Sci.*, 1966, **1**, 79-90.

21 C. A. Niedermeier, M. Rasander, S. Rhode, V. Kachkanov, B. Zou, N. Alford and M. A. Moram, *Sci Rep*, 2016, **6**, 31230.

22 D. Mourad, G. Czycholl, C. Kruse, S. Klembt, R. Retzlaff, D. Hommel, M. Gartner and M. Anastasescu, *Phys. Rev. B*, 2010, **82**, 165204.

23 S. H. Wei and A. Zunger, *Phys. Rev. Lett.*, 1996, **76**, 664-667.

24 R. D. Shannon, *Acta. Cryst.*, 1976, **A32**, 751-767.

25 F. Y. Jiang, D. W. Yang, Y. Y. Jiang, T. F. Liu, X. G. Zhao, Y. Ming, B. W. Luo, F. Qin, J. C. Fan, H. W. Han, L. J. Zhang and Y. H. Zhou, *J. Am. Chem. Soc.*, 2018, **140**, 1019-1027.

26 C. S. Ni, G. Hedley, J. Payne, V. Svrcek, C. McDonald, L. K. Jagadamma, P. Edwards, R. Martin, G. Jain, D. Carolan, D. Mariotti, P. Maguire, I. Samuel and J. Irvine, *Nat. Commun.*, 2017, **8**, 170.

27 H. T. Yin, J. L. Chen, Y. Wang, J. Wang and H. Guo, *Sci Rep*, 2017, **7**, 41567.

28 U. Dasgupta, A. Bera and A. J. Pal, *ACS Energy Lett.*, 2017, **2**, 582-591.

29 J. L. Bredas, *Mater. Horizons*, 2014, **1**, 17-19.

30 J. Endres, D. A. Egger, M. Kulbak, R. A. Kerner, L. F. Zhao, S. H. Silver, G. Hodes, B. P. Rand, D. Cahen, L. Kronik and A. Kahn, *J. Phys. Chem. Lett.*, 2016, **7**, 2722-2729.

31 A. L. Abdelhady, M. I. Saidaminov, B. Murali, V. Adinolfi, O. Voznyy, K. Katsiev, E. Alarousu, R. Comin, I. Dursun, L. Sinatra, E. H. Sargent, O. F. Mohammed and O. M. Bakr, *J. Phys. Chem. Lett.*, 2016, **7**, 295-301.

32 J. A. Van Vechten and T. K. Bergstresser, *Phys. Rev. B*, 1970, **1**, 3351-3358.

33 C. X. Ran, Z. X. Wu, J. Xi, F. Yuan, H. Dong, T. Lei, X. He and X. Hou, *J. Phys. Chem. Lett.*, 2017, **8**, 394-400.

34 Z. Zhang, X. W. Li, X. H. Xia, Z. Wang, Z. B. Huang, B. L. Lei and Y. Gao, *J. Phys. Chem. Lett.*, 2017, **8**, 4300-4307.

35 M. Q. Lyu, J. H. Yun, M. L. Cai, Y. L. Jiao, P. V. Bernhardt, M. Zhang, Q. Wang, A. J. Du, H. X. Wang, G. Liu and L. Z. Wang, *Nano Res.*, 2016, **9**, 692-702.

36 X. Chen, Y. Myung, A. Thind, Z. N. Gao, B. Yin, M. K. Shen, S. B. Cho, P. F. Cheng, B. Sadtler, R. Mishra and P. Banerjee, *J. Mater. Chem. A*, 2017, **5**, 24728-24739.

37 J. Teuscher, A. Ulianov, O. Muntener, M. Gratzel and N. Tetreault, *ChemSusChem*, 2015, **8**, 3847-3852.

38 C. L. Davies, M. R. Filip, J. B. Patel, T. W. Crothers, C. Verdi, A. D. Wright, R. L. Milot, F. Giustino, M. B. Johnston and L. M. Herz, *Nat. Commun.*, 2018, **9**, 293.

39 M. Pazoki, M. B. Johansson, H. M. Zhu, P. Broqvist, T. Edvinsson, G. Boschloo and E. M. J. Johansson, *J. Phys. Chem. C*, 2016, **120**, 29039-29046.

40 S. Oz, J. C. Hebig, E. W. Jung, T. Singh, A. Lepcha, S. Olthof, J. Flohre, Y. J. Gao, R. German, P. H. M. van Loosdrecht, K. Meerholz, T. Kirchartz and S. Mathur, *Sol. Energy Mater. Sol. Cells*, 2016, **158**, 195-201.

41 K. H. Kim, C. Takahashi, Y. Abe and M. Kawamura, *Optik*, 2014, **125**, 2899-2901.

42 W. M. Yang, L. X. Wang, X. C. Lu and Q. T. Zhang, *J. Mater. Sci.-Mater. Electron.*, 2015, **26**, 1113-1118.

Table of contents graphics and text
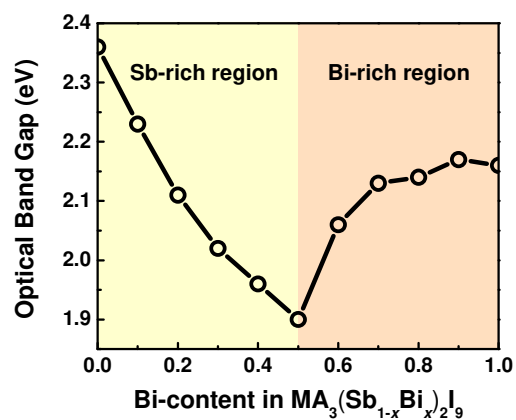
Bandgap bowing phenomenon has been observed in lead-free $MA_3Sb_2I_9$ perovskite upon isovalent substitution by bismuth (Bi^{3+}).